Chemical Engineering Science 320 (2026) 122490

Contents lists available at ScienceDirect

Chemical Engineering Science

journal homepage: www.elsevier.com/locate/ces

Tailoring N/O functionalities on porous carbons for high-efficiency CO_2 cycloaddition: Mechanistic insights and kinetic modeling

Jianhan Yang [a,b], Xueer Huang [c], Jiangnan Huang [a,*], Hao-Fan Wang [b], Hongjuan Wang [b], Hao Yu [b], Yonghai Cao [b,*]

[a] College of Chemistry and Chemical Engineering, Zhongkai University of Agriculture and Engineering, Guangzhou 510225, China
[b] School of Chemistry and Chemical Engineering, Guangdong Provincial Key Lab of Green Chemical Product Technology, South China University of Technology, Guangzhou 510640, China
[c] Collaborative Innovation Center of Chemical Science and Engineering, Key Laboratory for Green Chemical Technology of Ministry of Education, School of Chemical Engineering and Technology, Tianjin University, Tianjin 300072, China

ARTICLE INFO

Keywords:
Carbon catalyst
CO_2 cycloaddition
Carbonate
Nitrogen doping
Oxygen-containing group

ABSTRACT

The conversion of CO_2 into value-added chemicals is paramount for promoting environmental sustainability. Here, porous nitrogen-doped carbon materials (PNCMs) with adjustable nitrogen and oxygen content were synthesized and applied as catalysts for the cycloaddition of CO_2 to produce carbonates, achieving an outstanding carbonate yield up to 97%. Both experimental findings and DFT simulations demonstrated a synergistic interaction between nitrogen and oxygen functionalities in enhancing catalytic activity. Specifically, when normalized by specific surface area, the synergistic N/O functionalities on the carbon surface positively influenced catalytic performance, which was supported by the kinetic studies. Subsequently, organic molecules like phenol, nicotinic acid, 1,4-benzoquinone, and 3-hydroxypyridine were used as model catalysts to mimic the surface-active sites of PNCMs, leading to the development of an improved kinetic model that accurately predicted the performance of the carbon catalyst.

1. Introduction

The rising concentration of CO_2 from fossil fuel combustion and industrial processes has become a significant concern in the fields of global climate change and environmental sustainability (Liu et al., 2024). Consequently, there is considerable interest in developing effective strategies for the capture and utilization of CO_2. Among various approaches, the catalytic cycloaddition of CO_2 with epoxides yielding value-added chemicals, such as cyclic carbonates, stands out as a promising method (Marciniak et al., 2020; Tyagi et al., 2023). Cyclic carbonates, known for their high chemical stability and versatility, are widely used as the electrolytes in lithium-ion batteries, and the monomers for polycarbonate synthesis (Pescarmona, 2021), offering a sustainable alternative in the carbon cycle (Sathish et al., 2022).

In the field of catalysis, nanocarbon materials have attracted substantial attention due to their adjustable physic/chemical properties (Wang, Hong et al., 2020). Specifically, the nitrogen doping into the carbon framework enhances surface electron density and imparts Lewis basicity, which has shown remarkable potential in facilitating the cycloaddition of CO_2 (Lepre et al., 2022; Liu et al., 2019). For example, Ma et al. utilized N-doped carbon catalyst for CO_2 cycloaddition, achieving an 84.3 % yield of cyclic carbonate, six times higher than that without nitrogen doping (Ma et al., 2014). Samikannu et al. found that biochar with N-doped could achieve a 99 % yield of cyclic carbonate, whereas undoped carbon showed negligible activity (Samikannu et al., 2019). Despite these advancements, two challenges remain: (i) The complex relationship between the physical and chemical characteristics of the carbon surface and its catalytic performance is not fully understood. The interplay between nitrogen doping, surface functional groups (such as carboxyl, hydroxyl, and carbonyl groups), and surface area significantly influences the material's electron density and active site distribution, thereby affecting its catalytic activity (Cai et al., 2022; Liu et al., 2022; Yang et al., 2022; Zhang et al., 2020). However, N-doped carbons with similar nitrogen and oxygen content but different structures often exhibit varying activities in this process. For instance, nitrogen-doped carbon/silica nanosphere catalysts (e.g., M41/CN-RF and M-41/CN-PDA) with similar nitrogen content (2.16 % and 2.41 %) demonstrated significantly different catalytic performances in CO_2

* Corresponding authors.
E-mail addresses: huangjiangnan@zhku.edu.cn (J. Huang), meyhcao@scut.edu.cn (Y. Cao).

https://doi.org/10.1016/j.ces.2025.122490
Received 8 May 2025; Received in revised form 29 June 2025; Accepted 22 August 2025
Available online 23 August 2025
0009-2509/© 2025 Elsevier Ltd. All rights are reserved, including those for text and data mining, AI training, and similar technologies.

cycloaddition (78.9 % epoxide conversion for M-41/CN(b)-RF, compared to 68.4 % for M-41/CN(b)-PDA) (Liu et al., 2021). Similarly, N-doped porous carbon nanofibers (CNFW-600–2 and CNFW-650–2) with comparable oxygen (17.33 % and 18.20 % wt%) and nitrogen content (12.27 % and 10.05 % wt%) produced 86 % and 17 % cyclic carbonate yields, respectively (Li et al., 2016). Although differing reaction conditions may contribute to these variations, the structural diversity of N-doped carbon materials with substantial oxygen-containing groups likely plays a more critical role in influencing the reaction, particularly the complex interactions among nitrogen species, oxygen functionality, and surface area. (ii) Another key issue is the understanding of the kinetic features of the CO_2 cycloaddition over nanocarbon catalysts, which is essential for elucidating the reaction mechanism. Extensive studies have focused on the kinetic parameters of substrates and bulk catalysts. Typically, the kinetic parameters (i.e., apparent reaction rate constant, activation energy, and reaction order) of CO_2 cycloaddition catalyzed by carbon materials have been investigated, revealing a surface-dependent activity (Heydari et al., 2020; Luo et al., 2015; Zhang et al., 2018). However, a comprehensive kinetic model that accounts for the influence of nanocarbon material structure, surface chemistry, and reaction conditions remains elusive. The establishment of such a kinetic model is crucial for optimizing reaction parameters and designing more efficient catalysts.

In this study, porous nanocarbon flake materials (PNCMs) featuring precisely controlled nitrogen content and surface oxygen functional groups were synthesized via a one-pot process and employed as catalysts for the cycloaddition reaction of CO_2 with 1,2-butene oxide (BO). This approach enabled a systematic investigation into the individual contributions of surface functionalities and their synergistic effects on catalytic performance, thereby establishing a well-defined structure–activity relationship. Furthermore, we proposed a quantitative approach for determining the active sites on the surface of carbon materials and utilized organic molecular compounds as model catalysts to mimic the active sites on PNCMs. Consequently, the qualitative and quantitative challenges associated with the complex surface microstructure and heterogeneous distribution of active sites in carbon materials were effectively addressed. A kinetic model was also developed to quantitatively elucidate the influence of surface functionalities on the reaction.

2. Experimental section

2.1. Catalyst preparations

Typically, 6 g of $ZnCl_2$ and 2 g of chitosan (CS) were thoroughly mixed by grinding to serve as precursors, which was then annealed in a tubular furnace under a N_2 atmosphere for 60 min at 800 °C, with a heating rate of 5 °C/min. After cooling to room temperature, the synthesized carbon materials were immersed in a 1 M HCl solution with vigorous stirring to remove metal impurities. The mixture was then filtered and washed with deionized water several times until the solution reached a neutral pH. Subsequently, the solid materials were dried overnight at 60 °C under vacuum conditions. The obtained porous N-doped carbon material was denoted as PNCM-3@800. For the convenience of discussion, PNCM-3@800 could be noted as PNCM if applicable. Additional PNCMs samples were prepared by varying the mass ratio of $ZnCl_2$ to CS (ranging from 0.5 to 3) and the annealing temperature (ranging from 700 to 1000 °C), and these were denoted as PNCM-x@y, where x represents the mass ratio of $ZnCl_2$ to CS and y represents the annealing temperature. For comparison, nitrogen-doped carbon was also prepared using 2 g of CS as the sole precursor, following the aforementioned steps, and this material was denoted as NCM.

2.2. Catalytic performance

The catalytic activity tests were performed in batch mode using a stainless-steel micro-autoclave with a 50 mL capacity. Typically, 170 mmol of butylene oxide (BO), 20 mmol of 1,2-dichlorobenzene (used as an internal standard), 5.3 mmol of tetrabutylammonium bromide (TBAB), and 400 mg of catalyst were loaded into the micro-autoclave. The reaction system was purged and flushed with high-purity CO_2 (99.99 %) to remove any air, followed by a heating process. Once the desired temperature was reached, the autoclave was pressurized with CO_2 and maintained at this condition for 4 h. After the reaction was completed, the reactor was rapidly cooled down using an ice bath. The resulting mixture was diluted with N, N-dimethylformamide and then filtered. The liquid sample was analyzed using gas chromatography (Fuli-9790Plus) equipped with a capillary column (DB-1707) and a flame ionization detector. The temperature program was set as follows: initial temperature of 85 °C held for 1 min, followed by a heating rate of 15 °C/min to a final temperature of 265 °C. The injector temperature was set to 250 °C, and the detector temperature was set to 280 °C.

3. Results and discussion

3.1. Characterization and catalytic performance

Fig. 1**a** illustrates the schematic synthesis of porous carbon materials derived from chitosan (CS) and zinc chloride ($ZnCl_2$) as precursors. When CS was used alone, the resulting bulk nanocarbon material (NCM) exhibited an aggregated structure comprising irregular carbon sheets with a smooth surface and minimal defects and porosity (Fig. 1**b**). In contrast, the porous nanocarbon material (PNCM, representing PNCM@3–800), synthesized from a mixture of CS and $ZnCl_2$, displayed a flake-like and porous structure (Fig. 1**c**). The addition of $ZnCl_2$ as a pore-forming agent facilitated the creation of pores through sublimation and thermal etching processes, which react with the carbon materials (Dong et al., 2016; Lepre et al., 2022). HRTEM image revealed that the edges of PNCM featured a thin, curved few-layer graphene-like structure, with the surface uniformly decorated with numerous microporous architectures (Fig. 1**d**). The EDS mapping images indicated that carbon, nitrogen, and oxygen elements were uniformly distributed throughout the carbon material, likely due to the presence of numerous hydroxyl and acetylamino groups in the CS molecule (Fig. 1**e**) (Hu et al., 2022). XRD patterns exhibited two diffraction peaks at approximately 24° and 43°, referring to the graphitic (002) lattice planes and the disordered stacking of carbonaceous layers (1 0 1), respectively (Fig. 1**f**) (Mallesh et al., 2020; Serafin et al., 2023). Notably, no significant peaks corresponding to Zn nanoparticles were observed in these carbon catalysts. The specific surface area (SSA) of NCM and PNCM was 4.2 and 1645 $m^2\ g^{-1}$, respectively, indicating that the introduction of $ZnCl_2$ in the precursor enhanced the formation of microporous structures, which was also confirmed by the type IV curve with an H3 hysteresis loop observed in the N_2 adsorption/desorption isotherms (Chand et al., 2025) (Fig. 1**g**). This increase in specific surface area could be ascribed to the reorganization of the graphite structure following the evaporation of $ZnCl_2$ salt particles during the pyrolysis process, which facilitated an increase in pore volume (Cruz et al., 2017; Zhang et al., 2016). FTIR spectroscopy results demonstrated that both carbon samples exhibited several distinct peaks at approximately 1030–1170 cm^{-1}, 1530–1560 cm^{-1}, and 1590–1650 cm^{-1}, corresponding to C–O and C–N stretching vibrations, conjugated C–C stretching vibrations, and alkene (C=C) groups, respectively (Fig. 1**h**) (Kamran et al., 2022). The peak at 1620 cm^{-1} is attributed to prominent C=O (carbonyl) stretching vibrations (Wang, HY et al., 2020). Additionally, a strong O-H band was observed in the region of 3300–3500 cm^{-1} (Ding et al., 2024). A distinctive peak, attributed to the asymmetric stretching vibrations of adsorbed CO_2, was evident at approximately 2350–2400 cm^{-1} (Zhao et al., 2025). The content of these groups in PNCM increased significantly compared to that in NCM. The surface chemistry of both carbon materials was further analyzed using XPS technology (**Fig. S1a**). Typically, considerable amounts of N and O elements, derived from the hydroxyl groups and acetylamino groups in the CS molecule (Hu et al., 2022), were efficiently

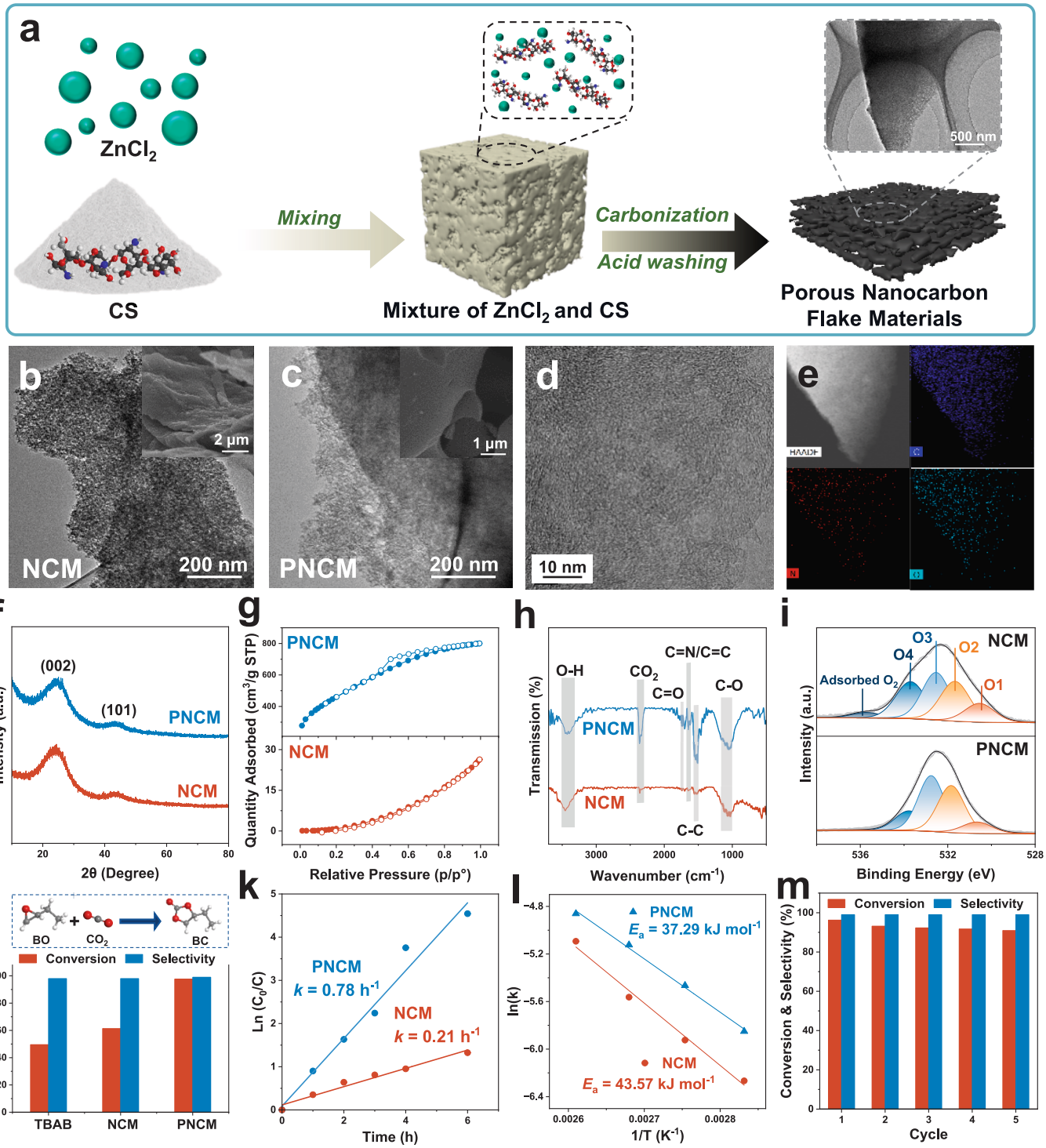

Fig. 1. (a) Illustration of the preparation of PNCMs derived from CS and $ZnCl_2$. SEM and TEM images of NCM (b) and PNCM (c). (d) HRTEM and (e) EDS images of PNCM. (f) XRD patterns, (g) N_2 adsorption/desorption isotherms, (h) FTIR spectra, (i) high-resolution of O_{1s} XPS spectra of NCM and PNCM. (j) The catalytic performance of carbon catalysts. Conditions: 400 mg catalyst, 170 mmol BO, 5.3 mmol TBAB, 1.0 MPa CO_2, 110 °C, 1100 rpm, 4 h. Pseudo first-order (k) and Arrhenius plot (l) of CO_2 cycloaddition catalyzed by NCM and PNCM. (m) Stability test of PNCM. Conditions: 400 mg catalyst, 170 mmol BO, 5.3 mmol TBAB, 1.0 MPa CO_2, 110 °C, 1100 rpm, 4 h.

incorporated into the carbon skeleton in both carbon catalysts. Notably, the introduction of $ZnCl_2$ in the precursor significantly increased the oxygen content from 6.96 at.% to 14.28 at.%, while not significantly altering the N content (6.72 at.% for NCM and 5.9 at.% for PNCM) (Fig. S1b). The introduction of $ZnCl_2$ into the precursor facilitated the production of surface defects on PNCM, which were easily occupied by oxygen-containing compounds derived from CS, leading to the formation of an increased number of oxygen functional groups (Chen et al., 2020; Hsan et al., 2020; Zhou et al., 2019). High-resolution O_{1s} XPS spectra with five deconvoluted peaks were observed for both NCM and PNCM, corresponding to carbonyl/quinone carbonyl (530.9 eV, O1), carboxyl (531.8 eV, O2), C-O-C (532.7 eV, O3), –OH (533.6 eV, O4), and absorbed O_2 (535.7 eV) (Fig. 1i) (Cai et al., 2022; Shafeeyan et al., 2010). Compared to NCM, the content of oxygen functionality

increased significantly in PNCM (**Table S1**), with C-O-C and carboxyl dominating the surface oxygen functionality. Furthermore, five peaks centered at 398.3 eV, 399.5 eV, 400.8 eV, 402.9 eV, and 404.9 eV in the high-resolution N1s XPS spectra were obtained, corresponding to pyridinic N (N1), pyrrolic N (N2), quaternary N (N3), N-oxide (N4), and chemisorbed N, respectively (**Fig. S2**) (Cao et al., 2013). In the current work, no significant difference in the content of nitrogen species between the two carbon materials was observed.

The catalytic performances for the CO_2 cycloaddition over both catalysts were evaluated. When NCM was used as a catalyst, a 61 % conversion of butylene oxide (BO) was obtained, slightly higher than the blank experiment (49 %). A significantly enhanced activity was observed over PNCM, with a BO conversion of 97 % (Fig. 1**j**), presenting a higher relative catalytic activity than reported carbon catalysts (**Table S2**). This indicates that the aforementioned surface modification, involving the creation of more micropores and an increase in surface oxygen content, is an efficient strategy to facilitate the reaction. The pseudo-first-order rate constants (k) for NCM and PNCM were 0.21 h^{-1} and 0.78 h^{-1}, respectively, further confirming that the high surface oxygen content of the carbon material significantly accelerates the CO_2 cycloaddition, given their similar N content (Fig. 1**k**). Meanwhile, this modification was also evident in the Arrhenius plot (Fig. 1**l**) which demonstrated that the apparent activation energy of PNCM was calculated to be 37.51 kJ mol^{-1}, lower than that of NCM (43.57 kJ mol^{-1}), confirming that PNCM can more efficiently lower the reaction barrier and accelerate the reaction. Furthermore, a stability test of PNCM was conducted (Fig. 1**m**). Before each test, PNCM was separated from the mixed solution and washed with ethanol to remove any residual reactants, followed by a drying process. The results demonstrated that after five consecutive test cycles, PNCM maintained a high catalytic activity, with a 91 % conversion of BO, showing no apparent decline in catalytic efficacy. Detailed characterizations of the recycled PNCM (r-PNCM) were carried out. The TEM image showed porous structure of the r-PNCM (**Fig. S3a**), similar to the pristine one. Meanwhile, no significant change of the XRD pattern and the FTIR spectra over r-PNCM were observed compared with the PNCM (**Fig. S3b and S3c**). Nevertheless, the SSA of r-PNCM was 1218.5 m^2 g^{-1} and the I_D/I_G value of r-PNCM was 0.97 (**Fig. S3d and S3e**), slightly lower than that of the fresh PNCM (1218.5 m^2 g^{-1} and 0.99). Furthermore, the XPS analysis revealed that the O content on r-PNCM decreased from 14.28 at.% to 7.72 at.% (**Fig. S3f**). Since the SSA and surface O content were highly related to the catalytic activity of carbon catalysts in the CO_2 cycloaddition, the aforementioned characterizations results showed that the decreased SSA and the number of oxygen functional groups on the surface of r-PNCM might be responsible for the slight decrease in activity observed during the five recycles.

3.2. DFT simulations

To elucidate the intrinsic role of surface functionality on carbon catalysts in the CO_2 cycloaddition, DFT simulations were conducted. According to the reaction mechanism of the CO_2 cycloaddition catalyzed by metal-free carbon materials, three key steps were considered to dominate the reaction (Ghosh et al., 2022; Hui et al., 2023). The first step involved the ring-opening reaction of epoxides to generate a transient alkoxide, intermediate 1 (C_4H_8OBr, Int.1). Subsequently, the addition of CO_2 to Int.1 occured, resulting in the formation of acyclic esters, intermediate 2 ($C_5H_8O_3Br$, Int.2). Finally, cyclic carbonates were formed through an intramolecular cyclization (Fig. 2**a**) (Samikannu et al., 2019). Among these steps, the ring-opening of epoxides is identified as the rate-determining step for this reaction (Chand et al., 2024a; Xia et al., 2024). Previous studies have demonstrated that when a nitrogen-doped nanocarbon was used as a catalyst, the surface Lewis acid site (typically, an oxygen-containing group) on the carbon materials acted as a hydrogen bond donor, facilitating the activation and ring-opening of epoxides by attacking the O atom in the epoxides (Yue et al., 2020). Meanwhile, nitrogen species, especially pyridinic nitrogen, were believed to act as anchors for CO_2 capture, efficiently facilitating the reactions (Li et al., 2016; Wu et al., 2021).

Herein, BO, CO_2, Int.1 (C_4H_8OBr) and Int.2 ($C_5H_8O_3Br$) were selected as model substrates, and four types of catalysts—pure graphite carbon (C1), carbon with a basic nitrogen site (C2), carbon with hydroxyl groups (C3), and carbon with both a basic nitrogen site and hydroxyl groups (C4) were established as model catalysts for the DFT simulations (Fig. 2**b** and **Table S3**). The adsorption energy ($E_{a,\ BO}$) between the BO molecule and the four models was calculated to be −0.26 eV (C1), −0.33 eV (C2), −0.88 eV (C3), and −0.87 eV (C4), respectively, indicating that hydroxyl groups were more favorable for interaction with BO through the formation of hydrogen bond (Heydari et al., 2020; Zhang et al., 2018). The $E_{a,\ CO2}$ for these four model catalysts was 0.48 eV (C1), −0.68 eV (C2), 0.29 eV (C3), and −0.62 eV (C4), respectively, confirming that the basic nitrogen species was the key site for the interaction with the CO_2 molecule. Furthermore, the $E_{a,\ Int.1}$ (−0.67 eV (C1), −0.59 eV (C2), −2.18 eV (C3), and −2.09 eV (C4)) and $E_{a,\ Int.2}$ (−0.84 eV (C1), −0.99 eV (C2), −2.24 eV (C3), and −1.84 eV (C4)) for these four model catalysts were simulated, showing that the presence of hydroxyl groups could markedly improve the interaction between Int.1, Int.2, and the carbon catalysts. Additionally, $E_{a,\ CO2}$ of the carbon with carbonyl group (C5) and the carbon with carboxyl group (C6) was calculated to be −0.33 eV (C5), and −0.46 eV (C6), respectively. $E_{a,\ BO}$ of the C6 was calculated to be −1.03 eV by forming hydrogen bond **(Table S4)**. This indicates that, in addition to the basic nitrogen species and hydroxyl groups, the other oxygen functional groups are equally capable of adsorbing CO_2 and BO molecules to some extent. Overall, the enhanced activity could be mainly attributed to the presence of surface oxygen functionality on the carbon material surface, and nitrogen doping could facilitate the adsorption of the CO_2 molecule.

In this work, the ring-opening of BO and the activation/addition of CO_2 as key intermediate reactions are believed to dominate the reaction, which traditionally needs to overcome a high reaction energy barrier (Guo et al., 2021). Therefore, DFT calculations were also performed for these two intermediate reactions in the presence of different catalysts (Fig. 2**c-d,** **Table S5**). A relatively low energy barrier was involved in the ring-opening reaction (TS1) of BO in the presence of hydroxyl groups (0.64 eV for C3 and C4), which was lower than the energy barrier in this transition state (TS1) without hydroxyl groups (1.87 eV for C1, 1.63 eV for C2). This difference primarily arose from the hydrogen bonding interaction between the hydroxyl group and BO, which redistributed electrons within the BO molecule. As a result, the carbon atom in BO with the least steric hindrance became more vulnerable to nucleophilic attack by the Br^- ion, ultimately reducing the energy barrier (Luo et al., 2023; Ye et al., 2022). For the interaction between Int.1 and CO_2, a higher barrier energy needed to be lowered to attack CO_2 by oxygen atom on the Int.1 molecule in the presence of hydroxyl groups (1.53 eV for C3, 1.30 eV for C4) compared to that without hydroxyl groups (0.30 eV for C1 and 0.24 eV for C2). It indicated that the addition of CO_2 and Int.1 to from Int.2 was the rate-determining step of the CO_2 cycloaddition with BO in the presence of hydroxyl group. This might be ascribed to the excessively strong adsorption between Int.1 and hydroxyl groups on the catalyst surface, hindering the desorption process and subsequent reaction with CO_2 (Tong et al., 2022). Meanwhile, the carbon catalyst with a nitrogen dopant, a Lewis basic site, could facilitate the adsorption of CO_2, where it modified the C=O bond angle to make it more active (Ghosh et al., 2022). Therefore, the presence of nitrogen dopant and oxygen functional groups facilitated two key intermediate reactions (ring opening of BO and activation/addition of CO_2), reducing the highest energy barrier of the reaction by about 20 %, thereby improving the overall reaction efficiency.

3.3. Structure-activity relationship

The preceding discussion has shown that the surface oxygen

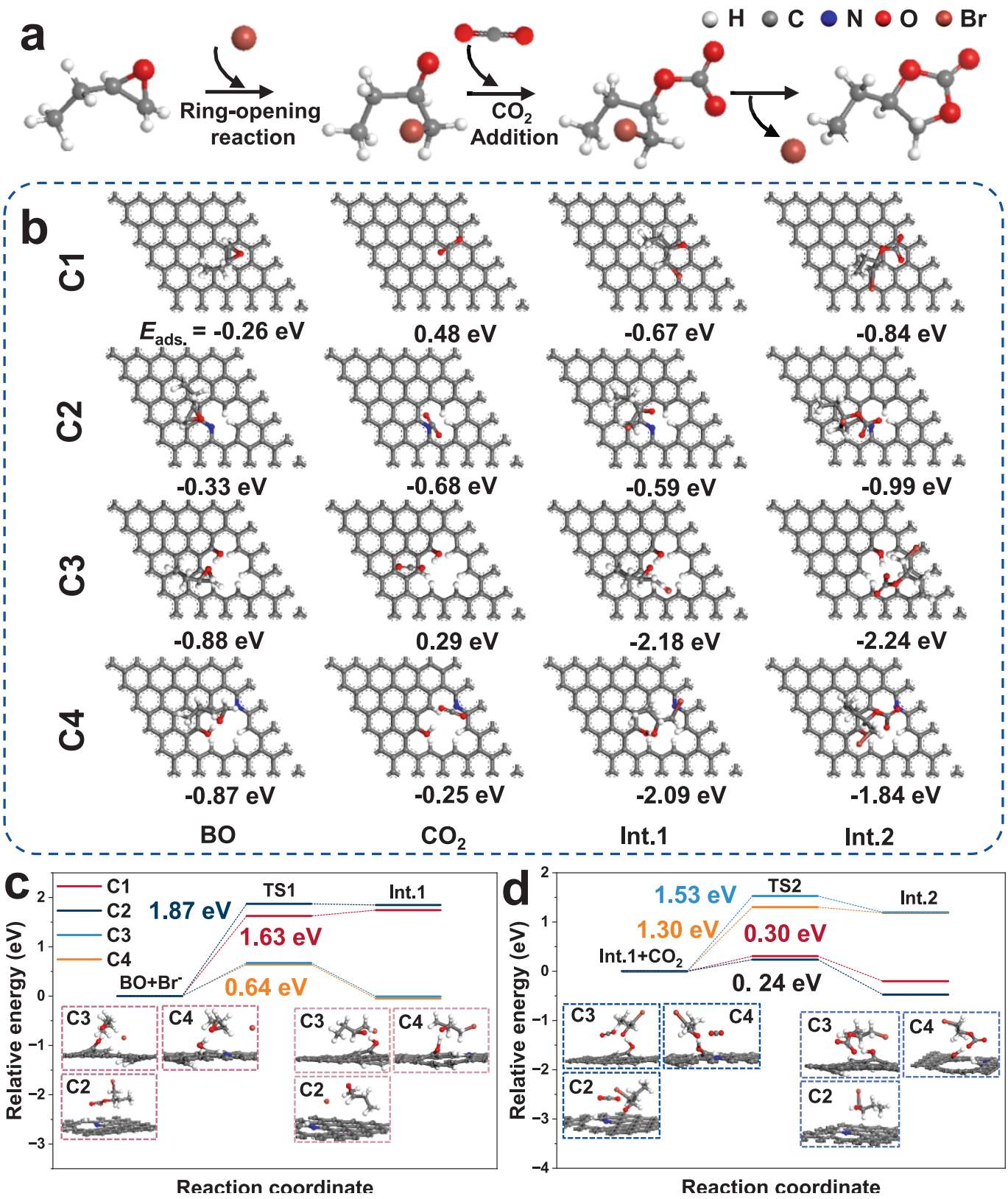

Fig. 2. (a) Schematic description of CO_2 cycloaddition with BO. (b)Structure optimization of BO, CO_2, Int.1 and Int.2 and carbon adsorbent from the DFT calculation. Energy diagram of (c) ring-opening reaction of BO to Int.1 and (d) CO_2 addition with Int.1 to Int.2.

functionality and N doping of porous nitrogen-doped carbon materials (PNCMs) exhibit a synergistic effect on the catalytic efficiency of CO_2 cycloaddition. Here, a series of PNCMs with tailored N and O contents were prepared (Table 1 and Fig. 3). TEM images demonstrated that the synthesized PNCMs under various conditions exhibited a flake structure with numerous mesopores on the surface (Fig. 3**a**), which contributed to the high specific surface area (SSA) of PNCMs (672.5–1645.0 $m^2\ g^{-1}$) (Fig. 3**b**). The more $ZnCl_2$ was used, the higher SSA could be obtained. Meanwhile, increasing the pyrolysis temperature (700–1100 °C) led to a gradual decrease in SSA across these carbon catalysts (from 1818.7 to 1258.5 $m^2\ g^{-1}$), likely due to the removal of surface functionalities and the remediation of surface defects under high temperature. The XRD pattern of PNCMs showed two broad peaks at 24° and 43°, further indicating the presence of numerous mesoporous carbon structures (**Fig. S4**) (Mallesh et al., 2020; Serafin et al., 2023). The I_D/I_G value of these carbon materials slightly increased from 0.92 to 0.99 with the increase in the amount of $ZnCl_2$ in the precursor (Fig. 3**c** and Table 1), indicating that the addition of $ZnCl_2$ facilitated the formation of pores and defects (Deng et al., 2015). Moreover, as the carbonization temperature increased, the I_D/I_G value decreased correspondingly, suggesting that higher carbonization temperatures led to a reduced defect density and enhanced graphitization on the PNCMs surface (Guo et al., 2020).

FTIR spectroscopy results demonstrated that similar contents of the surface groups were observed across these carbon catalysts (Fig. 3**d**). XPS survey results demonstrated that considerable N and O element contents were incorporated into PNCMs (Fig. 3**e and** Table 1). The application of $ZnCl_2$ did not significantly influence the contents of N (5.77–6.04 at.%) and O (16.03–17.63 at.%) elements. However, increasing the temperature caused a decrease in N content (from 7.50 to 3.05 at.%) and O content (from 14.28 to 5.14 at.%) functionality on the carbon surface, attributed to the low thermal stability of nitrogen dopants or oxygen functionality in carbon materials (Peng et al., 2019; Yang et al., 2022). The high-resolution N_{1s} spectra of PNCMs revealed that the main N species (N1, N2, and N3) dominated the PNCMs (Fig. 3**f**). The comparable decrease in N1 and N2 content indicated that high annealing temperatures benefited the transformation of N1 and N2 to N3 (Guo et al., 2023; Yang et al., 2019). Meanwhile, for the surface O functional groups, carbonyl/quinone carbonyl (O1), carboxyl (O2), ether (O3), and hydroxyl (O4) groups were present on the surface of all samples (Fig. 3**g**).

The catalytic performance of various PNCMs catalysts in the CO_2 cycloaddition was summarized (Table 1). Although these PNCMs exhibited differential surface chemical/physical features, they displayed considerably high catalytic efficiency for the CO_2 cycloaddition (93.87 ~ 97.67 % BO conversion). Here, the conversion was firstly increased with temperature from 700 °C to 800 °C then decreased at 900 °C and again increases at 1000 °C, which probably ascribed to the variations of SSA and N/O content, leading to the irregular BO conversion. Therefore, the initial rate normalized by the catalyst mass (R_g) and specific surface area (R_m) were correlated with the surface functionalities, which would be helpful in understanding the intrinsic role of the key activity sites. As shown in Fig. S5-S6, chaotic relationships were observed between R_g, R_m and O/N ratio or each single functionality, indicating that the catalytic activity of PNCMs could not be attributed to a single active site. However, with the increase of the surface element content (N and O), R_g and R_m generally showed an upward trend, even if this trend was not obvious, indicating that the catalytic efficiency of a catalyst highly relied on the SSA, which related to the number of surface-active sites. Therefore, the content of each single functionality (set as X) on the carbon surface was then normalized by the SSA (X/SSA) to represent the density of functionality content per unit surface area, which were plotted vs. R_g and R_m (Fig. S7). The obtained results demonstrated that the relationship between R_g and the ratio of each N or O component to SSA (Nx/SSA) was also chaotic, but obvious positive correlations between R_m and N1/SSA, O1/SSA, O3/SSA and O4/SSA were observed. Based on the aforementioned experimental and DFT results, the catalytic activity of porous PNCMs in the CO_2 cycloaddition was predominantly governed by PNCMs' SSA and the synergistic effect of partial N dopants and oxygen functional groups present on the PNCMs surface. Specifically, it was the quantity of N1, O1, O2, and O4 species exposed on the PNCMs surface, which played a crucial role in this reaction.

According to the literature, surface functionalities on carbon are considered key sites to promote the CO_2 cycloaddition reaction, which are usually defined as acidity sites (such as hydroxyl groups, lactones) and base sites (pyridinic N, amino groups) (Chand et al., 2021; Polidoro et al., 2022). For example, Zhang et al. demonstrated a positive correlation between hydroxyl group content and catalytic activity in the CO_2 cycloaddition (Zhang et al., 2018). Ye et al. confirmed surface carboxyl groups as active sites for CO_2 cycloaddition (Ye et al., 2022). Li et al. found a high dependence between the surface pyridinic N concentration and the catalytic performance of N-doped carbons (Li et al., 2016). Cheng et al. revealed the synergetic effect of pyridinic N and O functionalities would facilitate the reaction (Cheng et al., 2022). In the current study, the aforementioned results showed that O1, O2, O4, and N1 functionalities from XPS analysis displayed a considerable influence on the reaction (Fig. 3**f** and **g**). DFT simulations revealed that a synergistic enhancement between N sites and O functional groups on the

Table 1
Physical/chemical properties of PNCMs and their catalytic performance.

Catalyst	SSA[a] ($m^2\ g^{-1}$)	I_D/I_G[b]	*E.*[c] (at.%)		Deconvolution of N_{1s}[c] (at.%)			Deconvolution of O_{1s}[c] (at. %)				R_g[d] (mmol $min^{-1}\ g^{-1}$)	R_m[e] (10^{-2} mmol $min^{-1}\ m^{-2}$)	Con.[f] (%)	Sel.[f] (%)
			N_{1s}	O_{1s}	N1	N2	N3	O1	O2	O3	O4				
PNCM-0.5@800	672.51	0.92	5.98	16.03	2.03	1.58	1.70	1.23	4.63	7.01	2.80	10.29	1.53	93.87	>99
PNCM-1@800	1126.90	0.96	6.04	17.14	1.86	1.62	1.97	1.18	4.67	6.83	3.98	12.08	1.07	96.22	>99
PNCM-2@800	1605.80	0.96	5.77	17.63	2.08	1.56	1.47	1.91	4.23	7.25	3.75	13.87	0.86	96.34	>99
PNCM-3@800	1645.02	0.98	5.90	14.28	2.09	1.60	1.38	1.34	5.01	5.75	2.18	14.02	0.85	97.67	>99
PNCM-3@700	1818.71	0.99	7.50	11.90	2.66	2.18	1.84	1.44	3.62	5.58	1.05	11.73	0.65	96.67	>99
PNCM-3@900	1258.50	0.97	5.10	5.14	1.73	1.21	1.35	0.65	1.53	1.20	1.72	10.58	0.84	94.89	>99
PNCM-3@1000	1271.31	0.95	3.05	8.79	0.73	0.56	1.16	0.78	3.14	2.66	1.92	11.06	0.87	96.25	>99

[a] BET surface area. [b] Date from Raman spectra. [c] Date from XPS spectra (N1, N2, N3 represent as pyridinic N, pyrrolic N, and quaternary N, respectively; O1, O2, O3, O4 represent as carbonyl/quinone carbonyl, carboxyl, C–O–C, and –OH, respectively). [d] The initial rate normalized by the catalyst mass with < 20 % BO conversion. [e] The initial rate normalized by the specific surface area with < 20 % BO conversion. [f] Conditions: 400 mg catalyst, 170 mmol BO, 5.3 mmol TBAB, 1.0 MPa CO_2, 110 °C, 1100 rpm, 4 h.

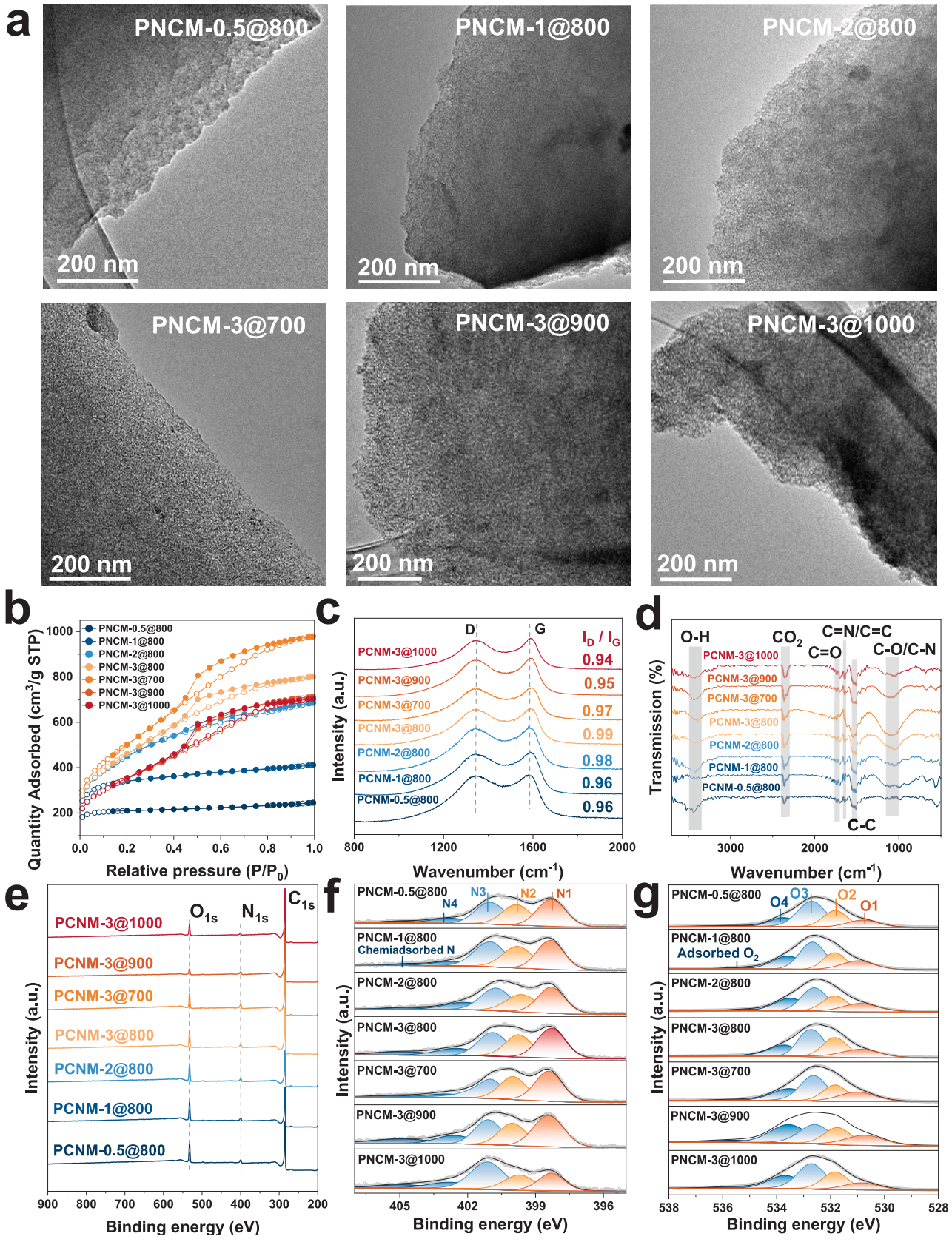

Fig. 3. (a) TEM images, (b) Raman spectra, (c) N_2 adsorption/desorption isotherm, (d) FTIR spectra, XPS survey (e) and high-resolution XPS spectra of N_{1s} (f) and O_{1s} (g) of PNCMs.

reaction was observed (Fig. 2**c and d**). Besides, volcanic curves of the relationship between R_g or R_m and (O + N)/SSA were obtained (Fig. 4**a and b**), indicating an underlying relationship between different functionalities and catalytic activity. Based on these results, a conjecture could be proposed that a combination of the amounts of O1, O2, O4, and N1 on the carbon surface might dominate the CO_2 cycloaddition reaction. Here, a well-defined dependence of the sum content of O1, O2, O4, and N1 on R_g and R_m was obtained (Fig. 4**c and d**), displaying a complex interaction between surface functionalities, which significantly modulated the overall activity.

3.4. Kinetic study

A kinetic investigation can provide valuable insights into the role of catalytic sites on the surface of PNCMs. Based on reported literature and previous discussions, it was evident that surface functionality, especially oxygen functionality and pyridinic N, played the crucial role in the reaction process. Using the chemical reaction equation provided in Fig. 5, a reaction rate equation for the cycloaddition of CO_2 (**Eq. (1)**) was derived. Given that CO_2 was supplied continuously throughout the reaction, allowing for a zero-order reaction for CO_2, **Eq. (1)** could be simplified to **Eq. (2)**.

$$R = -k_0[\mathrm{BO}]^{n_{BO}}[CO_2]^{n_{CO_2}}[\mathrm{TBAB}]^{n_{TBAB}}[\mathrm{PNCM}]^{n_{\mathrm{PNCM}}} \quad (1)$$

$$R = -k_0[\mathrm{BO}]^{n_{BO}}[\mathrm{TBAB}]^{n_{TBAB}}[\mathrm{PNCM}]^{n_{\mathrm{PNCM}}} \quad (2)$$

where n_{BO}, n_{TBAB}, and n_{OFGs} were represented as the reaction order for BO, TBAB, and PNCM, respectively. k_0 was the reaction rate constant, $\mathrm{mol^{1-n}\ L^{n-1}\ min^{-1}}$. [PNCM] referred to the total amount of O1, O2, O3 and N1 on the surface of PNCM, which was obtained from the BET and XPS analysis (Table S6).

In order to obtain the kinetic parameters and verify the rationality of the results, two methods were employed. The first method involved direct parameter determination from detailed experiments. These experiments varied the concentration of different substrates, such as BO, TBAB, and surface oxygen functionalities, while maintaining a BO conversion of less than 20 %. The logarithm of the reaction rate was plotted vs. the logarithm of the substrate concentration (Fig. 6**a-c**). The results indicated that n_{BO}, n_{TBAB}, and n_{PNCM} were 1.07, 0.39, and 0.32, respectively. By substituting these reaction orders and experimental values into **Eq. (2)**, we calculated k_0 to be 0.041 $\mathrm{mol^{-0.78}\ L^{0.78}\ min^{-1}}$.

The second method utilized the Runge-Kutta numerical integration via Python software to regress the collected kinetic experimental data (Fig. 6 **d-g** and **Table S7-S9**) (Mahadi et al., 2024; Zhong and Tian, 2012). The kinetic parameters obtained through this method closely matched those from the first method (Table 2). In this investigation, the decisive index ρ^2 was calculated to be 0.998 ($\rho^2 > 0.9$), the F-test value (F_c) was 3230.9, which exceeded the critical F-value ($F_{0.05} = 9.55$ under the current conditions), and the residual analysis R^2 was 0.995 (**Eq. (3)–(5)**. The uniform distribution of all data points within the 95 % confidence interval symmetrically flanking the diagonal (**Fig. S8a**) confirmed the feasibility of the obtained kinetic parameters for the CO_2 cycloaddition based on the Runge-Kutta numerical integration method.

$$\rho^2 = 1 - \frac{\sum_1^n (C_{e,i} - C_{c,i})^2}{\sum_1^n C_{e,i}^2} \quad (3)$$

$$F_c = \frac{\left[\sum_1^n C_{e,i}^2 - \sum_1^n (C_{e,i} - C_{c,i})^2\right]/\mathrm{P}}{\sum_1^n (C_{e,i} - C_{c,i})^2/\mathrm{n} - \mathrm{p}} \quad (4)$$

$$R^2 = \frac{\sum_1^n (C_{e,i} - C_{ave,i})^2 - \sum_1^n (C_{e,i} - C_{c,i})^2}{\sum_1^n (C_{e,i} - C_{ave,i})^2} \quad (5)$$

Where $C_{e,i}$, $C_{c,i}$ referred to the experimental value and the calculated value of the substance concentration in the reaction system, respectively. $C_{ave,i}$ was the average of the experimental value of the reaction substance, P and n referred to the number of parameters and the number

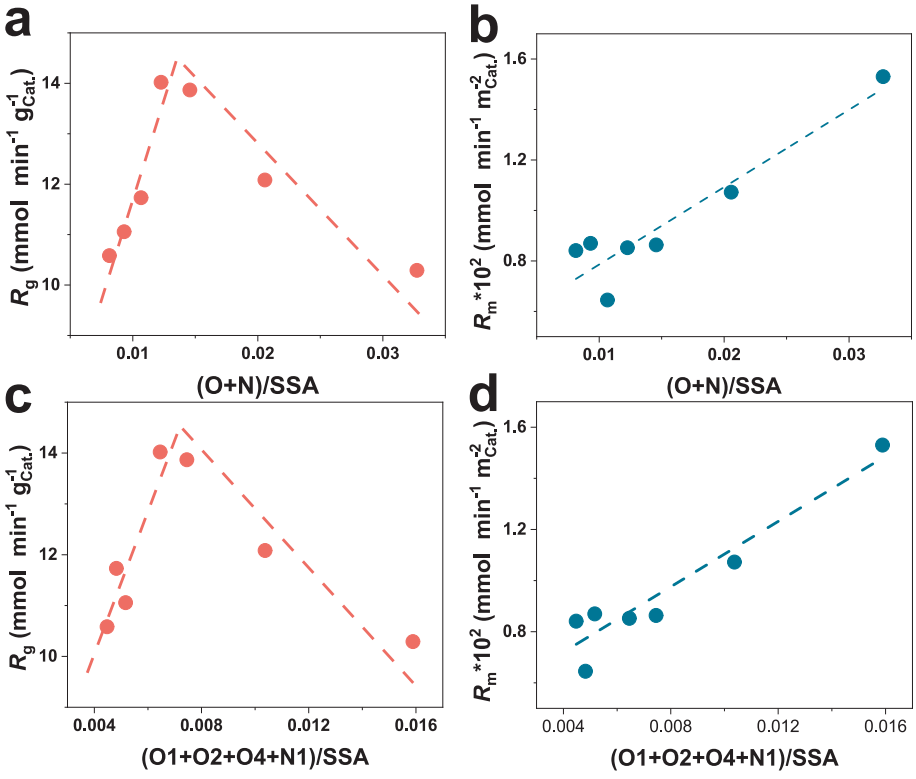

Fig. 4. Dependence of R_g on the value of (a) (O + N)/SSA and (b) (O1 + O2 + O4 + N1)/SSA of PNCMs. Dependence of R_m on the value of (c) (O + N)/SSA and (d) (O1 + O2 + O4 + N1)/SSA of PNCMs.

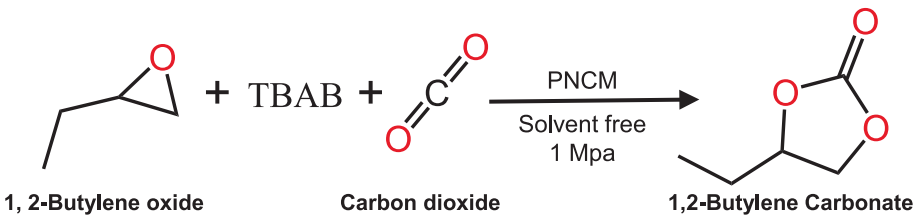

Fig. 5. Reaction equation of CO_2 cycloaddition with BO to BC catalyzed by PNCM.

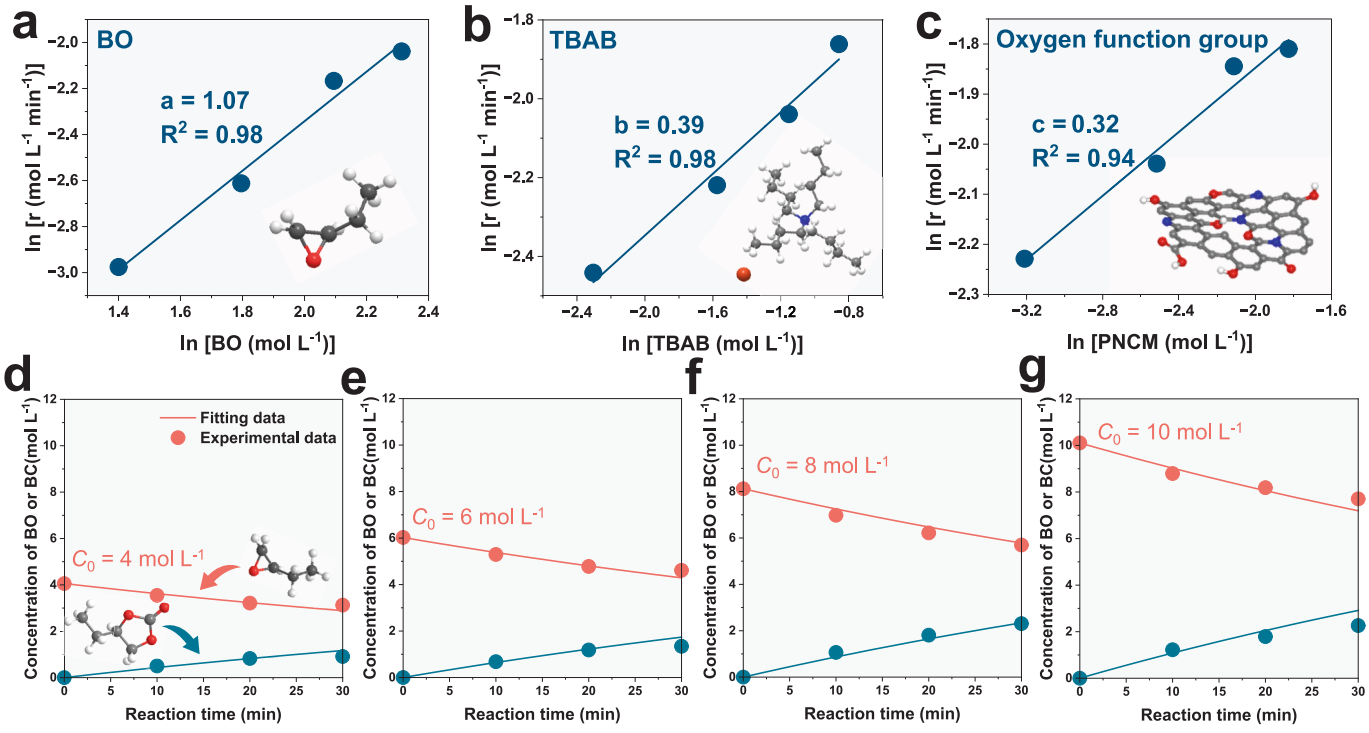

Fig. 6. Determination of reaction order of (a) BO, (b) TBAB and (c) oxygen function groups of CO_2 cycloaddition with BO catalyzed by PNCM. (d ~ g) The kinetic model fitted according to the Runge-Kutta method regression with different initial concentration of BO.

Table 2
Kinetic parameters of reaction obtain from experiment and Runge-Kutta method regression.

Catalyst	Kinetic parameters of reaction			
	k_0	n_{BO}	n_{TBAB}	$n_{PNCM\ or\ Cat.,x}$
PNCM	0.041	1.07	0.39	0.32
PNCM[a]	0.022	1.00	0.40	0.33
Phenol (Pe) [a]	0.49	1.00	0.41	0.65
Nicotinic acid (Na) [a]	0.08	1.01	0.45	0.36
1, 4-Benzoquinone (Bq) [a]	0.48	1.02	0.45	0.80
3-Hydroxypyridine (Hp) [a]	0.52	1.01	0.43	0.57

[a] Kinetic parameters obtained from Runge Kutta method.

of experiments, respectively.

Although we obtained kinetic parameters based on the amount of surface oxygen functionality, the diversity of oxygen functionalities still did not clarify which sites were responsible for the reaction. On a microscopic level, we identified four types of active sites on the surface of PNCM by DFT calculation and structure–activity relationship studies, including hydroxyl groups, carboxyl groups, carbonyl/quinone carbonyl, and pyridinic-N, as being responsible for catalytic activity. A kinetic study considering each site would be helpful to quantitatively reveal the effect of each site on the surface of these carbon catalysts. Therefore, based on a reaction rate equation for a single active site (**Eq. (6)**, we established a reaction rate equation (**Eq. (7)**, where the aforementioned four functionalities were denoted as Cat.1, Cat.2, Cat.3, and Cat.4, respectively.

$$R = -k_{Cat.}[BO]^{n_{BO,x}}[TBAB]^{n_{TBAB,x}}[Cat.n]^{n_{Cat.,x}} \tag{6}$$

$$R = -k_1[BO]^{n_{BO,1}}[TBAB]^{n_{TBAB,1}}[Cat.1]^{n_{Cat.,1}} - k_2[BO]^{n_{BO,2}}[TBAB]^{n_{TBAB,2}}[Cat.2]^{n_{Cat.,2}} - k_3[BO]^{n_{BO,3}}[TBAB]^{n_{TBAB,3}}[Cat.3]^{n_{Cat.,3}} - k_4[BO]^{n_{BO,4}}[TBAB]^{n_{TBAB,4}}[Cat.4]^{n_{Cat.,4}} \tag{7}$$

Where k_1, k_2, k_3, and k_4 were the reaction rate constant for each site, and $n_{BO,x}$, $n_{TBAB,x}$, and $n_{Cat.,x}$ refer to the reaction order of BO, TBAB and each active site, respectively.

In this reaction, given the excess concentration of BO and TBAB compared to the number of active sites on the catalyst surface, the values of $n_{BO,1} \sim n_{BO,4}$ and $n_{TBAB,1} \sim n_{TBAB,4}$ were similar. Consequently, **Eq. (7)** could be simplified to **Eq. (8)**:

$$R = -k_5[BO]^{n_{BO}}[TBAB]^{n_{TBAB}}\left(\frac{k_1}{k_5}[Cat.1]^{n_{Cat.,1}} + \frac{k_2}{k_5}[Cat.2]^{n_{Cat.,2}} + \frac{k_3}{k_5}[Cat.3]^{n_{Cat.,3}} + \frac{k_4}{k_5}[Cat.4]^{n_{Cat.,4}}\right) \tag{8}$$

Compared with some materials such as carbon nitride and metal–organic frameworks, which have highly regular microstructures and specific active site distributions (Chand et al., 2024b; Eskemech et al.,

2024), the surface structure and physicochemical properties of carbon materials, such as PNCM in this work, are more complex. Since precisely modulating each surface functionality while keeping others unchanged on nanocarbons was the great challenge, we utilized small organic molecules such as 1,4-benzoquinone (BQ), nicotinic acid (NA), phenol (Ph), and 3-hydroxypyridine (HP) as model functionalities to simulate the surface oxygen functionalities of PNCM (corresponding to O1, O2, O4, and N1 functionalities). Before solving **Eq. (8)**, the kinetic parameters for each organic model catalyst in this reaction were obtained using the Runge-Kutta regression via **Eq. (6)**. The results from this method closely matched the experimental data (Fig. 7 **a-l and** Table S10). Here, ρ^2 was 0.997 ($\rho^2 > 0.9$), the F_c was 2224.7 ($> 100F_{0.05}$), and R^2 was 0.990. All data points were well fitted within symmetrical 95 % confidence intervals (Fig. S8b), confirming the feasibility of the obtained kinetic parameters of these model catalysts for the CO_2 cycloaddition. The kinetic parameters of the four model catalysts are shown in Table 2, which were close to the apparent kinetic parameters (**Eq. (2)**, verifying the rationality of the obtained kinetic model. Notably, the activation energies for these four organic model catalysts were 54.5 kJ mol^{-1}, 76.8 kJ mol^{-1}, 12.7 kJ mol^{-1}, and 46.7 kJ mol^{-1} (Table S11), also close to that of PNCMs (Fig. 1**l**), indicating that these organic model catalysts could be used to simulate the surface

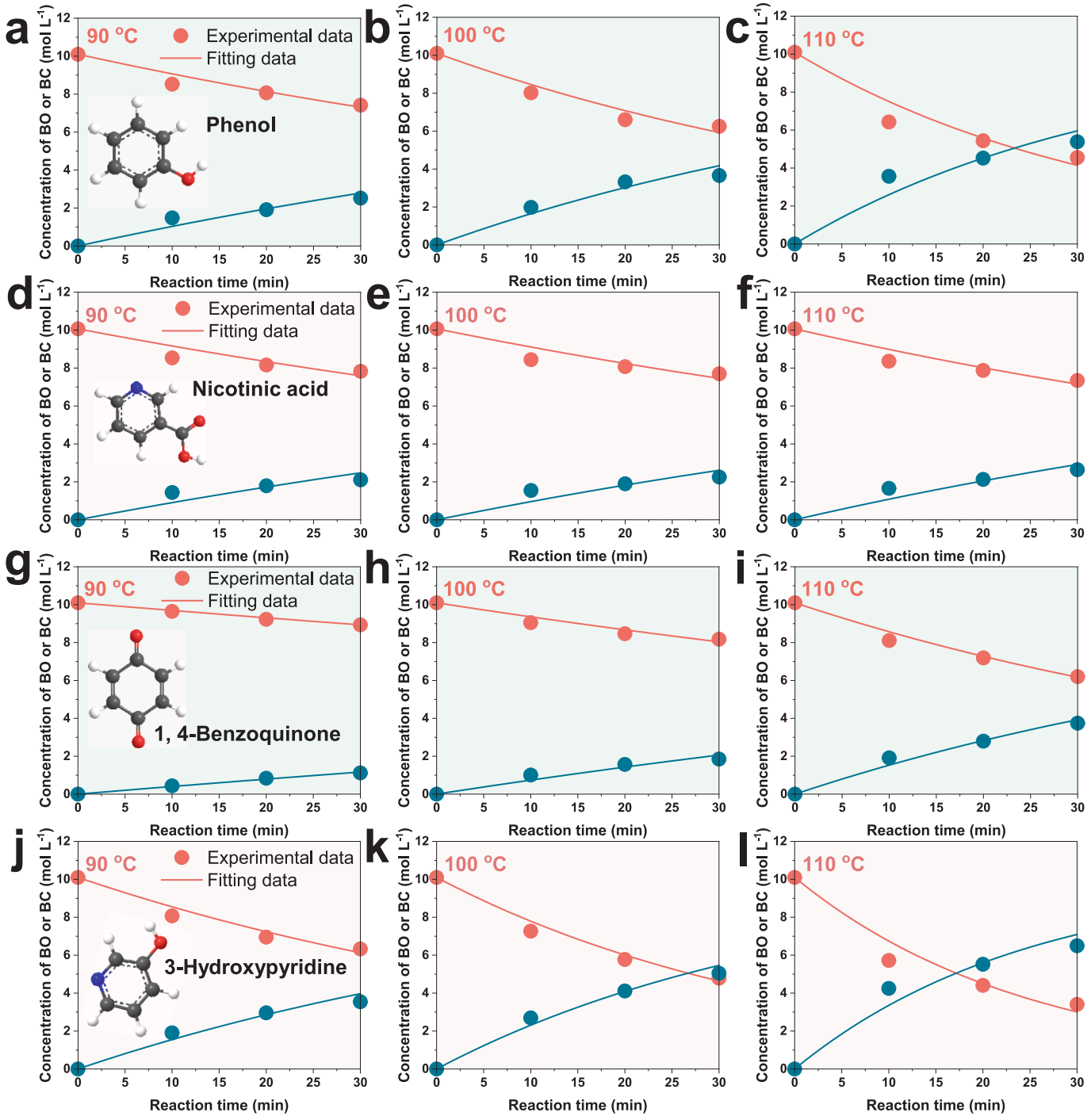

Fig. 7. Effect of temperature on the catalysis of this reaction by phenol (Ph) (a-c), nicotinic acid (Na) (d-f), 1, 4-benzoquinone (Bq) (g-i) and 3-hydroxypyridine (Hp) (g-l). Conditions: 0.06 mmol model catalysts, 170 mmol BO, 3.6 mmol TBAB, 1.0 MPa CO_2, 1100 rpm.

functionalities on the PNCMs for the CO_2 cycloaddition.

By integrating the obtained kinetic models and parameters, the reaction model based on the four organic model catalysts could be established as **Eq. (9)**.

$$R = -k_5[\mathrm{BO}]^1[\mathrm{TBAB}]^{0.40}\left[\left(\frac{k_1}{k_5}[\mathrm{Cat.1}]^{0.65}+\frac{k_2}{k_5}[\mathrm{Cat.2}]^{0.36}+\frac{k_3}{k_5}[\mathrm{Cat.3}]^{0.80}+\frac{k_4}{k_5}[\mathrm{Cat.4}]^{0.57}\right)\right] \quad (9)$$

Subsequently, the reaction rate constants ($k_1 \sim k_5$) were determined through regression analysis using the Runge-Kutta method with the previous experimental data (Fig. 8**a-d** and Table S6-9). The refined reaction rate constants were obtained as follows: $k_1 = 0.045\ \mathrm{mol}^{-1.05}\ \mathrm{L}^{1.05}\ \mathrm{min}^{-1}$, $k_2 = 0.043\ \mathrm{mol}^{-0.81}\ \mathrm{L}^{0.81}\ \mathrm{min}^{-1}$, $k_3 = 0.002\ \mathrm{mol}^{-1.25}\ \mathrm{L}^{1.25}\ \mathrm{min}^{-1}$, $k_4 = 0.003\ \mathrm{mol}^{-1.00}\ \mathrm{L}^{1.00}\ \mathrm{min}^{-1}$, and $k_5 = 0.014\ \mathrm{mol}^{-1.40}\ \mathrm{L}^{1.40}\ \mathrm{min}^{-1}$. All data points were uniformly distributed within a symmetrical 95 % confidence interval flanking the diagonal, with ρ^2, F_c and R^2 being 0.998, 353.0, and 0.995, demonstrating strong agreement between the model's calculated values and experimental data (Fig. S8c). Hence, the reaction rate equation could be described as **Eq. (10)**. Furthermore, when considering the reaction temperature, **Eq. (11)** was derived by incorporating an activation energy term (Arrhenius equation) (Table S12), which could be used to predict the concentration of different substrates under various conditions. Here, NCM, a catalyst with a more distinct structure from PNCM (Fig. 1), was used as the model catalyst. The surface functionality of NCM was quantitatively determined (Table S6), and the corresponding activation energy (E_a) was applied to the reaction (Fig. 1**l**). In the current study, experiments were conducted at 80 ~ 110 °C with different initial concentrations of BO. The predicted data from the kinetic model closely matched the experimental data (Fig. 8**e-h** and Table S13**)**, with ρ^2, F_c and R^2 being 0.998, 331.4, and 0.995. The symmetrical dispersion of all model-derived data points within the 95 % confidence interval around the unity line substantiates excellent concordance between predicted values and experimental observations (Fig. S8d). These results further confirm that the established kinetic model and selected organic molecule catalysts in this work can be effectively applied to simulate the diverse nanocarbon catalysts in the CO_2 cycloaddition process.

$$R = -0.014[BO]^1[TBAB]^{0.40}(3.21[\mathrm{Cat.1}]^{0.65}+3.28[\mathrm{Cat.2}]^{0.36}+0.14[\mathrm{Cat.3}]^{0.80}+0.21[\mathrm{Cat.4}]^{0.57}) \quad (10)$$

$$R = -A_5 e^{\left(\frac{-E_{a,5}}{RT}\right)}[\mathrm{BO}]^1[\mathrm{TBAB}]^{0.40}\left[\frac{A_1}{A_5}e^{\left(\frac{-E_{a,1}+E_{a,5}}{RT}\right)}[\mathrm{Cat.1}]^{0.65}+\frac{A_2}{A_5}e^{\left(\frac{-E_{a,2}+E_{a,5}}{RT}\right)}[\mathrm{Cat.2}]^{0.36}+\frac{A_3}{A_5}e^{\left(\frac{-E_{a,3}+E_{a,5}}{RT}\right)}[\mathrm{Cat.3}]^{0.80}+\frac{A_4}{A_5}e^{\left(\frac{-E_{a,4}+E_{a,5}}{RT}\right)}[\mathrm{Cat.4}]^{0.57}\right] \quad (11)$$

Where $E_{a,1} \sim E_{a,5}$, and $A_1 \sim A_5$ were the activation energy and pre-exponential factor of model catalysts, respectively.

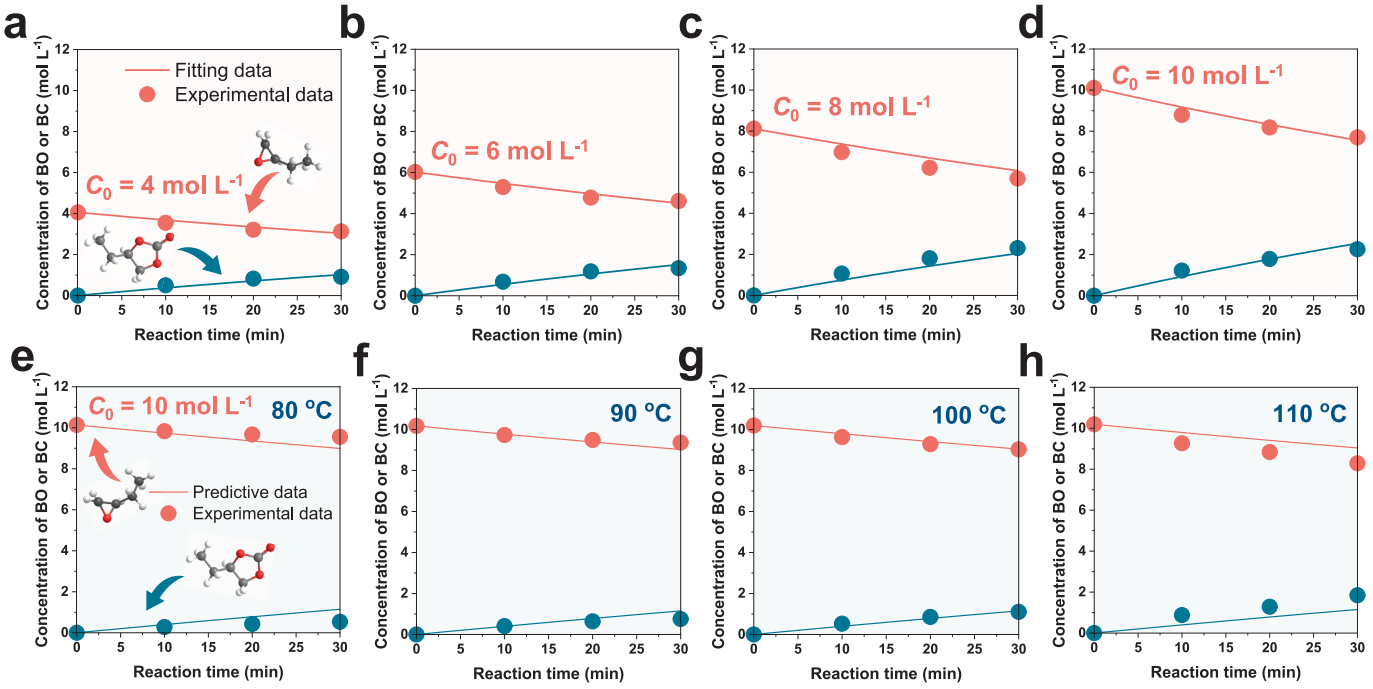

Fig. 8. (a ~ d) Results of the empirical formulas for PNCM fitted according to the Runge-Kutta method regression with different initial concentration of BO. (e ~ h) Calculated and predicted values of the empirical formulas for NCM in different reaction temperatures.

4. Conclusions

In summary, we successfully synthesized PNCMs materials with tunable surface N and O functionalities, which were subsequently utilized as unique catalysts for CO_2 cycloaddition. These catalysts achieved an outstanding carbonate yield of 97 % with an apparent k of 0.78 h^{-1}, which was much higher than that of NCMs (61 % and 0.21 h^{-1}). The considerable stability of PNCM was observed as 91 % conversion was observed after 5 cycles. The N dopants and oxygen-containing groups on the PNCM surface might be responsible for the high activity. DFT simulations revealed that the synergistic incorporation of pyridinic nitrogen, carbonyl, carboxyl and hydroxyl group on the carbon surface would reduce the maximum energy barrier for CO_2 cycloaddition from 1.63 eV to 1.30 eV, which was supported by structure–activity relationship studies as well. To further elucidate the catalytic role of these surface functionalities, we also developed a comprehensive kinetic model that accounts for their effects, from which key kinetic parameters were extracted. Organic molecules (phenol, nicotinic acid, 1,4-benzoquinone, and 3-hydroxypyridine) were used as model catalysts to mimic the behavior of the carbon-based catalysts in CO_2 cycloaddition. The kinetic model was refined using experimental data from these organic systems, and its validity was confirmed through experiments with an alternative carbon catalyst. The obtained rate constants ($k_1 \sim k_5$) for these organic model catalyzed-system were 0.045 $mol^{-1.05}$ $L^{1.05}$ min^{-1}, 0.043 $mol^{-0.81}$ $L^{0.81}$ min^{-1}, 0.002 $mol^{-1.25}$ $L^{1.25}$ min^{-1}, 0.003 $mol^{-1.00}$ $L^{1.00}$ min^{-1}, and 0.014 $mol^{-1.40}$ $L^{1.40}$ min^{-1}. This study provides novel insights into how surface functionalities influence the catalytic performance of carbon materials.

CRediT authorship contribution statement

Jianhan Yang: Writing – original draft, Validation, Methodology, Investigation, Data curation. **Xueer Huang:** Software, Methodology. **Jiangnan Huang:** Writing – review & editing, Software, Resources, Data curation. **Hao-Fan Wang:** Resources, Methodology. **Hongjuan Wang:** Resources, Methodology. **Hao Yu:** Resources, Methodology. **Yonghai Cao:** Writing – review & editing, Resources, Project administration, Methodology.

Declaration of competing interest

The authors declare that they have no known competing financial interests or personal relationships that could have appeared to influence the work reported in this paper.

Acknowledgements

We would like to acknowledge the financial support from the National Natural Science Foundation of China (22272056), Guangdong Basic and Applied Basic Research Foundation (2022A1515140108), CNPC Innovation Found (2021DQ02-0704) Research Fund Program of Guangdong Provincial Key Laboratory of Fuel Cell Technology (FC202305), and the start-up fund from Zhongkai College of Agricultural Engineering.

Appendix A. Supplementary data

The additional experimental section, characterizations and discussion can be found in the Supporting Information. Supplementary data to this article can be found online at https://doi.org/10.1016/j.ces.2025.122490.

Data availability

Data will be made available on request.

References

Cai, Z., Liu, D., Huang, J., Feng, J., Wang, H., Yang, G., Peng, F., Cao, Y., Yu, H., 2022. Solvent-Free Production of ε-Caprolactone from Oxidation of Cyclohexanone Catalyzed by Nitrogen-Doped Carbon Nanotubes. Ind. Eng. Chem. Res. 61 (5), 2037–2044.

Cao, Y., Yu, H., Tan, J., Peng, F., Wang, H., Li, J., Zheng, W., Wong, N., 2013. Nitrogen-, phosphorous- and boron-doped carbon nanotubes as catalysts for the aerobic oxidation of cyclohexane. Carbon 57, 433–442.

Chand, H., Allasia, N., Cipriano, L.A., Liberto, G.D., Kwon, I.S., Zhang, M., Pacchioni, G., Krishnan, V., Vilé, G., 2025. Synergistic Effects in a Nitrogen-Coordinated Zinc Single-Atom Catalyst for Efficient CO2 Cycloaddition. ChemCatChem 17 (5), e202401768.

Chand, H., Bhumla, P., Goswami, S., Allasia, N., Vilé, G., Bhattacharya, S., Krishnan, V., 2024a. Facile Low-Temperature synthesis of novel carbon nitrides for efficient conversion of carbon dioxide into Value-Added chemicals. J. Colloid Interface Sci. 673, 943–957.

Chand, H., Choudhary, P., Kumar, A., Krishnan, V., 2021. Atmospheric pressure conversion of carbon dioxide to cyclic carbonates using a metal-free Lewis acid-base bifunctional heterogeneous catalyst. J. CO2 Util. 51, 101646.

Chand, H., Kumar, A., Goswami, S., Krishnan, V., 2024b. Comparison of catalytic activity of graphitic carbon nitrides derived from different precursors for carbon dioxide conversion. Fuel 357, 129757.

Chen, W., Gong, M., Li, K., Xia, M., Chen, Z., Xiao, H., Fang, Y., Chen, Y., Yang, H., Chen, H., 2020. Insight into KOH activation mechanism during biomass pyrolysis: Chemical reactions between O-containing groups and KOH. Appl. Energy 278, 115730.

Cheng, B.H., Deng, L.J., Jiang, J., Jiang, H., 2022. Catalytic cycloaddition of CO2 to epoxides by the synergistic effect of acidity and alkalinity in a functionalized biochar. Chem. Eng. J. 442, 136265.

Cruz, G., Kubonová, L., Aguirre, D., Matejová, L., Peikertová, P., Troppová, I., Cegmed, E., Wach, A., Kustrowski, P., Gomez, M., Obalová, L., 2017. Activated Carbons Prepared from a Broad Range of Residual Agricultural Biomasses Tested for Xylene Abatement in the GaS Phase. ACS Sustain. Chem. Eng. 5 (3), 2368–2374.

Deng, X., Zhao, B., Zhu, L., Shao, Z., 2015. Molten salt synthesis of nitrogen-doped carbon with hierarchical pore structures for use as high-performance electrodes in supercapacitors. Carbon 93, 48–58.

Ding, T., Xu, W., Zhang, J., Zhang, X., Sun, H., Shi, L., Wei, J., Xu, D., Zhang, S., Duan, X., Zhang, J., Wang, S., Sun, H., 2024. Green preparation of fiberboard waste derived N-doped carbon catalysts with tailored properties for efficient hydrogenation reduction of nitroaromatics. Chem. Eng. J. 489, 151197.

Dong, X., Lu, A., He, B., Li, W., 2016. Highly microporous carbons derived from a complex of glutamic acid and zinc chloride for use in supercapacitors. J. Power Sources 327, 535–542.

Eskemech, A., Chand, H., Karmakar, A., Krishnan, V., Koner, R.R., 2024. Zn-MOF as a Single Catalyst with Dual Lewis Acidic and Basic Reaction Sites for CO2 Fixation. Inorg. Chem. 63 (8), 3757–3768.

Ghosh, A., Reddy, G.N., Siddhique, P.K.M., Chatterjee, S., Bhattacharjee, S., Maitra, R., Lyubimov, S.E., Arzumanyan, A.V., Naumkin, A., Bhaumik, A., Chowdhury, B., 2022. Fabrication of a hollow sphere N,S co-doped bifunctional carbon catalyst for sustainable fixation of CO2 to cyclic carbonates. Green Chem. 24 (4), 1673–1692.

Guo, L., Lamb, K.J., North, M., 2021. Recent developments in organocatalysed transformations of epoxides and carbon dioxide into cyclic carbonates. Green Chem. 23 (1), 77–118.

Guo, R., Liu, X., Wen, B., Liu, F., Meng, J., Wu, P., Wu, J., Li, Q., Mai, L., 2020. Engineering Mesoporous Structure in Amorphous Carbon Boosts Potassium Storage with High Initial Coulombic Efficiency. Nano-Micro Letters 12 (1), 148.

Guo, Y., Chang, Q., Shi, Z., Xie, J., Yun, J., Zhang, L., Wu, H., 2023. Regulating conduction and polarization losses by adjusting bonded N in N-doped Cu/CuO/C composites. J. Colloid Interface Sci. 639, 444–453.

Heydari, P., Hafizi, A., Rahimpour, M.R., Khalifeh, R., 2020. Experimental investigation of improved graphene oxide as an efficient catalyst for the sustainable chemical fixation of CO2 with epoxides. J. Environ. Chem. Eng. 8 (6), 104568.

Hsan, N., Dutta, P.K., Kumar, S., Das, N., Koh, J., 2020. Capture and chemical fixation of carbon dioxide by chitosan grafted multi-walled carbon nanotubes. J. CO2 Util. 41, 101237.

Hu, T., Zeng, L., Li, Y., Wu, Y., Zhu, Z., Zhang, Y., Tian, D., Gao, C., Li, W., 2022. Multifunctional chitosan non-woven fabrics modified with terylene carbon dots for selective detection and efficient adsorption of Cr(VI). Chem. Eng. J. 432, 134202.

Hui, W., Shi, L., Xu, X.Y., Wang, H.J., Sun, M.S., Tao, D.J., 2023. Rapid and effective cycloaddition of environmentally diluted CO2 catalyzed by hierarchical porous ionic carbon at atmospheric conditions. J. Environ. Chem. Eng. 11 (2), 109458.

Kamran, U., Rhee, K., Lee, S., Park, S., 2022. Solvent-free conversion of cucumber peels to N-doped microporous carbons for efficient CO2 capture performance. J. Clean. Prod. 369, 133367.

Lepre, E., Rat, S., Cavedon, C., Seeberger, P.H., Pieber, B., Antonietti, M., Lopez-Salas, N., 2022. Catalytic Properties of High Nitrogen Content Carbonaceous Materials. Angew. Chem. Int. Ed. 62 (2), e202211663.

Li, Y., Zou, B., Hu, C.W., Cao, M.H., 2016. Nitrogen-doped porous carbon nanofiber webs for efficient CO2 capture and conversion. Carbon 99, 79–89.

Liu, D., Kang, S.M., Xu, Y.J., Duan, P.G., Chen, S.X., 2021. Core-shell catalyst with synergistic hydroxyl and nitrogen active sites for CO2 cycloaddition. J. Environ. Chem. Eng. 9 (6), 106452.

Liu, X., Zhou, Y., Wang, C.L., Liu, Y., Tao, D.J., 2022. Solvent-free self-assembly synthesis of N-doped ordered mesoporous carbons as effective and bifunctional materials for CO2 capture and oxygen reduction reaction. Chem. Eng. J. 427, 130878.

Liu, Y.X., Wang, H.H., Zhao, T.J., Zhang, B., Su, H., Xue, Z.H., Li, X.H., Chen, J.S., 2019. Schottky Barrier Induced Coupled Interface of Electron-Rich N-Doped Carbon and Electron-Deficient Cu: In-Built Lewis Acid-Base Pairs for Highly Efficient CO2 Fixation. J. Am. Chem. Soc. 141 (1), 38–41.
Liu, Z., Deng, Z., Davis, S.J., Ciais, P., 2024. Global carbon emissions in 2023. Nat. Rev. Earth Env. 5 (4), 253–254.
Luo, L., Yang, C., Liu, F., Zhao, T., 2023. Heteroatom-N,S co-doped porous carbons derived from waste biomass as bifunctional materials for enhanced CO2 adsorption and conversion. Sep. Purif. Technol. 320, 124090.
Luo, R., Zhou, X., Fang, Y., Ji, H., 2015. Metal- and solvent-free synthesis of cyclic carbonates from epoxides and CO2 in the presence of graphite oxide and ionic liquid under mild conditions: A kinetic study. Carbon 82, 1–11.
Ma, X., Zou, B., Cao, M., Chen, S.L., Hu, C., 2014. Nitrogen-doped porous carbon monolith as a highly efficient catalyst for CO2 conversion. J. Mater. Chem. A 2 (43), 18360–18366.
Mahadi, M.B., Azmi, I.S., Kadir, M.Z.A., Mohamed, N., Rahman, M.A., Jalil, M.J., 2024. Sustainable epoxidation of expired palm oil–derived oleic acid via in situ peracid mechanism with applied ion resin Amberlite IR-120H: from waste to wealth. Biomass Convers. Bior. 14 (15), 17395–17403.
Mallesh, D., Anbarasan, J., Kumar, P., Upendar, K., Chandrashekar, P., Rao, B., Linglan, N., 2020. Synthesis, characterization of carbon adsorbents derived from waste biomass and its application to CO2 capture. Appl. Surf. Sci. 530, 147226.
Marciniak, A.A., Lamb, K.J., Ozorio, L.P., Mota, C.J.A., North, M., 2020. Heterogeneous catalysts for cyclic carbonate synthesis from carbon dioxide and epoxides. Curr. Opin. Green Sust. 26, 100365.
Peng, A., Qi, S., Liu, X., Xue, D., Peng, S., Yu, G., Liu, X., Sun, L., 2019. N-doped porous carbons derived from a polymer precursor with a record-high N content: Efficient adsorbents for CO2 capture. Chem. Eng. J. 372, 656–664.
Pescarmona, P., 2021. Cyclic carbonates synthesised from CO2: Applications, challenges and recent research trends. Curr. Opin. Green Sust. 29, 100457.
Polidoro, D., Perosa, A., Rodriguez-Castellon, E., Canton, P., Castoldi, L., Rodriguez-Padron, D., Selva, M., 2022. Metal-Free N-Doped Carbons for Solvent-Less CO2 Fixation Reactions: A Shrimp Shell Valorization Opportunity. ACS Sustain. Chem. Eng. 10 (41), 13835–13848.
Samikannu, A., Konwar, L.J., Maki-Arvela, P., Mikkola, J.P., 2019. Renewable N-doped active carbons as efficient catalysts for direct synthesis of cyclic carbonates from epoxides and CO2. Appl. Catal. B: Env. 241, 41–51.
Sathish, M., Gopinath, A., Madhan, B., Subramanian, V., Rao, J., 2022. Cyclic carbonate: A green multifunctional agent for sustainable leather manufacture. J. Clean. Prod. 356, 131818.
Serafin, J., Dziejarski, B., Junior, O.F.C., Srenscek-Nazzal, J., 2023. Design of highly microporous activated carbons based on walnut shell biomass for H2 and CO2 storage. Carbon 201, 633–647.
Shafeeyan, M., Daud, W., Houshmand, A., Shamiri, A., 2010. A review on surface modification of activated carbon for carbon dioxide adsorption. J. Anal. Appl. Pyrolysis 89 (2), 143–151.
Tong, H., Qu, Y., Li, Z., He, J., Zou, X., Zhou, Y., Duan, T., Liu, B., Sun, J., Guo, K., 2022. Halide-free pyridinium saccharinate binary organocatalyst for the cycloaddition of CO2 into epoxides. Chem. Eng. J. 444, 135478.
Tyagi, P., Singh, D., Malik, N., Kumar, S., Malik, R., 2023. Metal catalyst for CO2 capture and conversion into cyclic carbonate: Progress and challenges. Mater. Today 65, 133–165.
Wang, H., Deng, H., He, Y., Huang, L., Wei, D., Hao, T., Wang, S., Jin, L., Zhang, L., 2020a. Facile and sustainable synthesis of slit-like microporous N-doped carbon with unexpected electrosorption performance. Chem. Eng. J. 396, 125249.
Wang, H., Shao, Y., Mei, S., Lu, Y., Zhang, M., Sun, J.k., Matyjaszewski, K., Antonietti, M., Yuan, J, 2020b. Polymer-Derived Heteroatom-Doped Porous Carbon Materials. Chem. Rev. 120 (17), 9363–9419.
Wu, X., Guan, R., Zheng, W.T., Huang, K., Liu, F., 2021. Developing porous organic polymers as precursors of nitrogen-decorated micro-mesoporous carbons for efficient capture and conversion of carbon dioxide. J. Mater. Sci. 56 (15), 9315–9329.
Xia, L., Chen, H., Wang, W., Jia, X., Zhang, D., Wang, L., Wu, P., Li, L., Huang, J., 2024. Facet and dual vacancy engineering-boosting BiOBr for enhanced CO2 and epoxide cycloaddition reaction under mild and cocatalyst-free conditions: Double substrate active sites and activated surface bromine ions synergy. J. Mater. Sci. Technol. 202, 39–49.
Yang, C.L., Zhao, T.X., Pan, H.Y., Liu, F., Cao, J.X., Lin, Q., 2022. Facile preparation of N-doped porous carbon from chitosan and NaNH2 for CO2 adsorption and conversion. Chem. Eng. J. 432, 134347.
Yang, L., Xu, G., Ban, J., Zhang, L., Xu, G., Lv, Y., Jia, D., 2019. Metal-organic framework-derived metal-free highly graphitized nitrogen-doped porous carbon with a hierarchical porous structure as an efficient and stable electrocatalyst for oxygen reduction reaction. J. Colloid Interface Sci. 535, 415–424.
Ye, Y., Liang, L., Zhang, X., Sun, J., 2022. Simple carbonaceous-material-loaded mesoporous SiO2 composite catalyst for epoxide-CO2 cycloaddition reaction. J. Colloid Interface Sci. 610, 818–829.
Yue, Z., Pudukudy, M., Chen, S., Liu, Y., Zhao, W., Wang, J., Shan, S., Jia, Q., 2020. A non-metal Acen-H catalyst for the chemical fixation of CO2 into cyclic carbonates under solvent- and halide-free mild reaction conditions. Appl. Catal. A: Gen. 601, 117646.
Zhang, G., Luo, H., Li, H., Wang, L., Han, B., Zhang, H., Li, Y., Chang, Z., Kuang, Y., Sun, X., 2016. ZnO-promoted dechlorination for hierarchically nanoporous carbon as superior oxygen reduction electrocatalyst. Nano Energy 26, 241–247.
Zhang, J., Zhang, G., Jin, S., Zhou, Y., Ji, Q., Lan, H., Liu, H., Qu, J., 2020. Graphitic N in nitrogen-Doped carbon promotes hydrogen peroxide synthesis from electrocatalytic oxygen reduction. Carbon 163, 154–161.
Zhang, S., Zhang, H., Cao, F., Ma, Y., Qu, Y., 2018. Catalytic Behavior of Graphene Oxides for Converting CO2 into Cyclic Carbonates at One Atmospheric Pressure. ACS Sustain. Chem. Eng. 6 (3), 4204–4211.
Zhao, S., Wang, K., Yang, B., Sun, Z., Zhao, Y., 2025. Synergistic catalysis of dual-sites promoted cycloaddition of CO2 with epoxides. Fuel 381, 133305.
Zhong, W., Tian, Z., 2012. The Chemical Kinetic Numerical Computation and Kinetic Model Parameters Estimating of Parallel Reactions with Different Reaction Orders. Mater. Sci. Tech. 560–561, 1126–1132.
Zhou, J., Wang, M., Li, X., 2019. Promising biomass-derived nitrogen-doped porous carbon for high performance supercapacitor. J. Porous Mater. 26 (1), 99–108.